8-2019

Radiation Pattern Reconfigurable Horn Antenna Based on Parasitic Layer Concept

Mehmet Tanagardi
Utah State University

RADIATION PATTERN RECONFIGURABLE HORN ANTENNA BASED ON PARASITIC LAYER CONCEPT

by

Mehmet Tanagardi

A thesis submitted in partial fulfillment
of the requirements for the degree

of

MASTER OF SCIENCE

in

Electrical Engineering

Approved:

Bedri A. Cetiner, Ph.D. Major Professor	Ryan Davidson, Ph.D. Committee Member
T.C. Shen, Ph.D. Committee Member	Richard S. Inouye, Ph.D. Vice Provost for Graduate Studies

UTAH STATE UNIVERSITY
Logan, Utah

2019

ABSTRACT

Radiation Pattern Reconfigurable Horn Antenna

Based on Parasitic Layer Concept

by

Mehmet Tanagardi, Master of Science

Utah State University, 2019

Major Professor: Bedri A. Cetiner, Ph.D.
Department: Electrical and Computer Engineering

The main objective of this thesis is to study an approach to achieve radiation pattern reconfiguration for the horn antenna. A radiation pattern reconfigurable horn antenna (RHA) is capable of steering its main beam in three directions in the semi-sphere space corresponding to $\theta \in \{-25^o, 0^o, 25^o\}$, is presented. The RHA consists of a driven X-band (10 GHz - 11.5 GHz) horn antenna, reconfigurable parasitic layer and dielectric loaded truncated pyramid (DLTP). The surface of the parasitic layer consists of metallic pixels, which are interconnected by PIN diode switches enabling to configure the surface geometry, where each geometry corresponds to a mode of operation. The working mechanism of the presented reconfigurable antenna is analyzed by both analytical calculations and full-wave simulations. The results indicate that from 10 GHz to 11.5 GHz a directivity of $\sim$ 14 dB is achieved in all modes of operation.

(51 pages)

PUBLIC ABSTRACT

Radiation Pattern Reconfigurable Horn Antenna
Based on Parasitic Layer Concept
Mehmet Tanagardi

In recent years, multi-functional reconfigurable antennas (MRA) has attracted much attention in wireless communication. The reconfigurable antenna can adapt itself with changing system conditions, and it can provide different multi-functionalities which can give better system performances. Instead of using multiple antennas, a single reconfigurable antenna can provide the same performance and occupy less space. By using the parasitic layer technique, an antenna can be turned into a reconfigurable antenna. The main objective of this thesis is to study radiation pattern reconfiguration of the horn antenna by using the parasitic layer concept. The MRA consists of a single horn, dielectric loaded truncated pyramid (DLTP), and the parasitic layer. The antenna that is chosen in this thesis is the horn antenna because it provides high directivity. DLTP is used for magnification purpose. The results show that three modes of operations that provide better performances compared to the single horn antenna are achieved.

I am dedicating this thesis to my mother, my brother, and my friends. They have provided me patience, encouragement, and support.

ACKNOWLEDGMENTS

I would like to express my appreciation to my advisor Dr. Bedri Cetiner, for his support, guidance, advice, and understanding. He has helped me academically and provided support to me to become a professional in the engineering environment. His advice on both research and my career have been invaluable. I am also thankful to committee members: Dr. T.C. Shen and Dr. Ryan Davidson for their support.

I am also grateful to Merve Kandemir and Mehmet Ozturk. They provided me support and encouragement. I want to thank the staff of the Department of the Electrical and Computer Engineering of the Utah State University for their support at any time. I would especially want to thank Joshua Perkins, who is my colleague and friend, for his friendship and support.

Mehmet Tanagardi

CONTENTS

Page

LIST OF TABLES

LIST OF FIGURES

ACRONYMS

MRA	Multi-functional Reconfigurable Antenna
RHA	Reconfigurable Horn Antenna
SRF	Self Resonant Frequency
EM	Electromagnetic
HFSS	High Frequency Structure Simulator
PRS	Partially Reflective Surface
HPBW	Half Power Beam-width
RF	Radio Frequency
DLTP	Dielectric Loaded Truncated Pyramid
FNBW	First Null Beamwidth
DC	Direct Current
SDL	Space Dynamics Laboratory
QTC	Quick Turn Circuit
SMD	Surface Mount Device
ABS	Acrylonitrile Butadiene Styrene

CHAPTER 1

Introduction

1.1 Introduction

Wireless communication systems are expanding toward multitasking environments for applications where users need to be linked to various services and connections. To this end, an antenna, which has different functionalities, is advantageous. A single multifunctional reconfigurable antenna (MRA) capable of generating multiple modes of operations in terms of frequency, polarization and radiation pattern can provide [1–3] cost, size, and performance advantages for RF wireless transceivers. Among various approaches and technologies in developing MRAs, reconfigurable parasitic layer technique has attracted much attention [2]. In this approach, as the parasitic and the driven antenna layers are separated from each other, the design constraints on driven antenna due to switching circuitry, which is placed on the parasitic layer, are removed. This enables achieving the optimum individual designs for both driven antenna and parasitic layers. Also, the manufacturing procedure could become more flexible allowing separate fabrication of these two parts [1].

1.2 Motivation

The main motivation behind this project is to show that parasitic layer technology can also work with high directive antennas. Also, to improve the gain from previously presented MRAs is the main idea behind this work. In this project, the horn antenna which is employed as a driven element is used together with the parasitic layer. Also, it has been shown [4] that dielectric material loaded structure provides better impedance matching and further gain enhancement for horn antenna. Therefore, the horn antenna is used in conjunction with a dielectric material loaded structure as an additional layer to advance the performances further.

1.3 Thesis Organization

In Chapter two, the literature review about multifunctional reconfigurable antennas is presented. Motivations behind the designing of radiation pattern reconfigurable horn antenna are emphasized.

The third chapter starts with the design of a single horn antenna by providing analytical calculations and full-wave simulations. In the fourth chapter, the design of the dielectric loaded truncated pyramid is presented. The simulated results and analytical calculations are given and discussed. The Chapter five presents the parasitic layer design steps that are used in MRA. The working mechanism of parasitic layer is analyzed and compared by both analytical calculations and full-wave simulations. In Chapter six, the overall combination of previously designed MRA components to get the finalized version of MRA is presented. The overall MRA results are given and discussed.

The Chapter seven introduces fabrication and assembly processes of the designed MRA. The methods are given step by step. The manufacturer information of the lumped components and the companies that can get individual MRA component done are provided.

Chapter eight concludes the thesis and points out the future work.

CHAPTER 2

Literature Review

2.1 Introduction

MRAs are one of the most promising ideas for the wireless networks which can adapt itself dynamically to environmental conditions, policies, network capabilities, and other parameters [1]. The main advantage of MRA technology is the capability of adjusting operation frequency, radiation pattern, and polarization by a single antenna element [5]. For the high directive antennas such as horn antenna, there is a challenge to maintain gain for their reconfigured modes. This type of antennas must provide excellent aperture efficiency, low losses, and low back-side radiation for their reconfigured or steered radiation patterns [6]. Therefore, developing an MRA that can provide these features is the primary motivation behind this research project.

2.2 Parasitic Layer Concept

The parasitic layer is located in the reactive field, where the reconfigurable surface is divided into multiple pixels that can be connected or disconnected by various switches. Therefore, the surface geometry of this layer can be modified, where each configuration corresponds to different modes of operation. With the parasitic layer approach, the reconfiguration capability can be added to the existing non-reconfigurable antenna, and it has clear advantages from fabrication, integration, and biasing perspectives [1].

2.3 MRA Examples

In the literature, there are some proposed designs for radiation pattern reconfiguration of the horn antenna. Mechanical reconfiguration [7] has been studied on horn antennas.

This approach has the disadvantage of being slow to achieve all configurations. Another method is the agile plasma wall technique [6], where the plasma is used in order to ensure modification of the radiation pattern electrically. However, this design is only able to modify the half power beam-width (HPBW). The parasitic layer can be easily used to reconfigure the radiation pattern of a horn antenna.

There are also proposed MRA examples that provide reconfiguration by the parasitic layer concept. In [8], the reconfiguration method based on the use of pixel surfaces as parasitic elements for patch antenna that is operating at 10 GHz is presented. The parasitic layer is used to provide nine different beam steering modes. However, the simple method is introduced with a large number of switches compared to proposed MRA. Another study [9] has optimized the number of pixels and provided the gain enhancement. However, since the used antennas are a patch in the given examples, provided gain is a quite low gain compared to proposed MRA. Not only patch antennas, but dipole antennas are also used together with the parasitic layer to create MRA structure as it is shown in the study [10]. However, the design is intricate due to its geometry and cannot provide high gain as proposed MRA.

Another approach to control the antenna radiation pattern is to employ a partially reflective surface (PRS) with a driven antenna. It is shown in [11] that PRSs can be used to dynamically control the beam of the antennas by changing the reflective properties of the surface. These antennas can offer high gain; nonetheless, a large number of switches are needed to tune the surface impedance.

2.4 Conclusion

To sum up, the parasitic layer based radiation pattern reconfigurable horn antenna is needed. It is also shown in [4] that using dielectric material loaded structures with horn antennas can enhance antenna gain and improve input impedance matching. Therefore, in this project, the dielectric material loaded structure is used together with parasitic pixel layer and its location, geometry, dimensions, and material properties are analyzed to enhance antenna performance.

CHAPTER 3

Horn Design

This chapter focuses on the design of the horn antenna which is used in the multifunctional reconfigurable antenna as a driven element. During the design process, we used the full-wave electromagnetic (EM) simulations [12] and analytical calculations. Horn antennas are popular, and they are one of the most used antennas at microwaves. Some of the main characteristics of horn antennas are simplicity, versatility, significant gain, proper matching, and good overall performance, as well as low side lobes [13]. Horn antennas usually have low loss hence the high efficiency which makes their directivity almost the same as their gain. There are several types of horn antennas which can be given an example as E-plane, H-plane or pyramidal horn antennas as shown in Fig. 3.1. If the opening is flared in the H-field direction, it is called an H-plane horn as in Fig. 3.1(a) If the opening is flared in the E-field direction, it is called an E-plane horn as in Fig. 3.1(b). If the opening is flared in both directions, then it is called a pyramidal horn as in Fig. 3.2(c) [14].

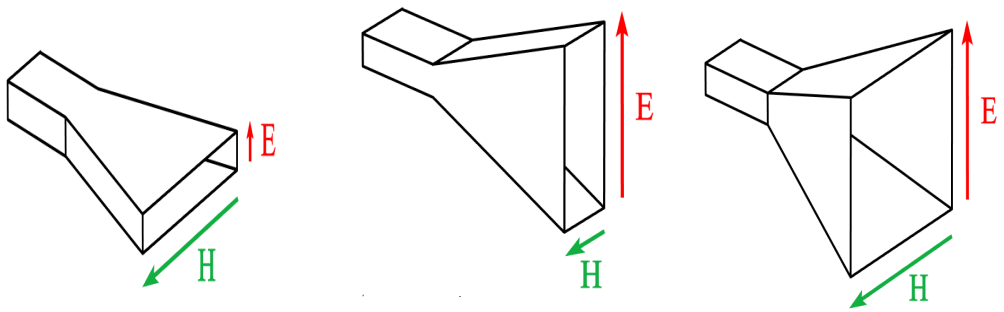

(a) (b) (c)

Fig. 3.1: a) H-plane b) E-plane and c) Pyramidal horn.

3.1 Horn Antenna Architecture

In this project, we targeted the design to be practical, so the horn antenna which

is commercially available was chosen. The Pasternack's WR-90 waveguide standard gain horn antenna [15] operating at X-band is selected as a driven element in this project. The dimensions of the chosen horn antenna can be seen in Fig. 3.2.

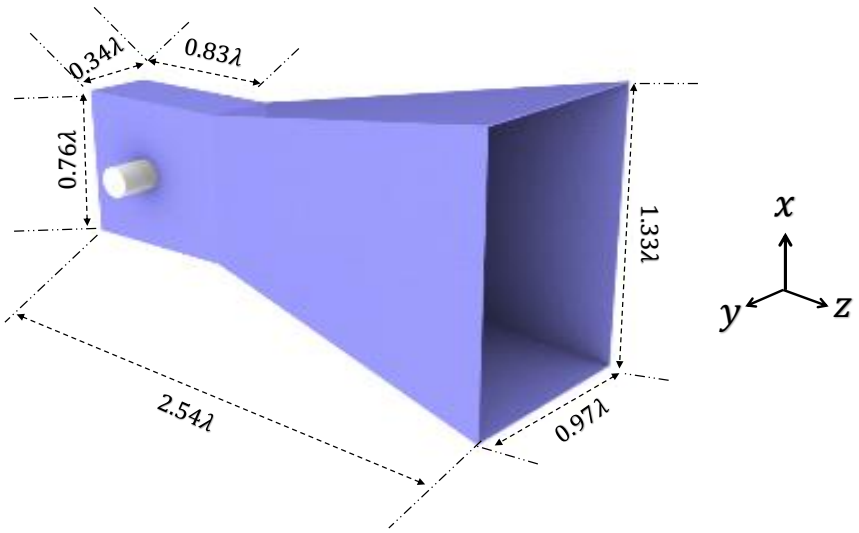

Fig. 3.2: Horn antenna dimensions (λ denotes wavelength in the air at 10 GHz).

3.2 Rectangular Waveguide and Transverse Electromagnetic Modes

The horn antenna has WR-90, which is a rectangular waveguide. Waveguides can have different shapes, but the rectangular waveguides can provide high power levels, and they usually offer low losses [16]. Horn antennas and a variety of components such as couplers and, insulators have an interface to the rectangular waveguides [17]. The horn antenna design starts with waveguide design, and the feeding waveguide is chosen according to the frequency range of interest [14]. The dimensions of the WR-90 waveguide is given in Fig. 3.3.

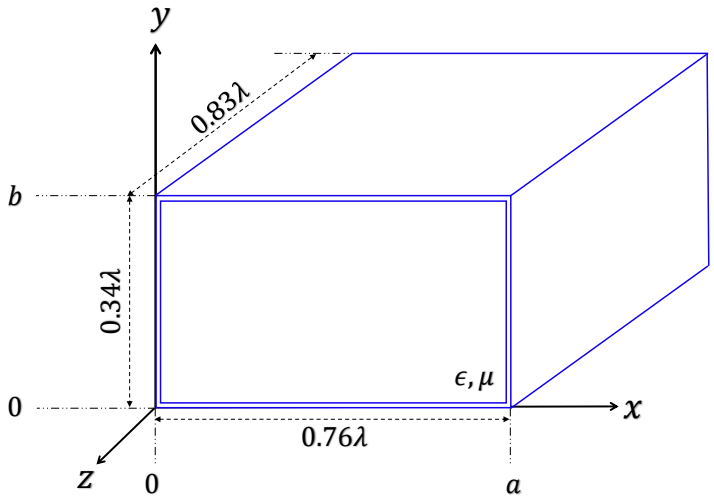

Fig. 3.3: WR-90 waveguide dimensions (λ denotes wavelength in the air at 10 GHz).

$$f_{c_{mn}} = \frac{1}{2\sqrt{\mu\epsilon}}\sqrt{(\frac{m}{a})^2 + (\frac{n}{b})^2} = \frac{c}{2\sqrt{\mu_r\epsilon_r}}\sqrt{(\frac{m}{a})^2 + (\frac{n}{b})^2} \tag{3.1}$$

The cutoff frequency expression for a particular mode in the rectangular waveguide is given in equation (3.1). In (3.1), a and b are the dimensions of the WR-90, c is the speed of light, and $\mu_r = \epsilon_r = 1$ for the air, and m and n denote the possible modes. By using the dimensions of the WR-90 waveguide, the cut-off frequencies of the modes are listed in Table 3.1. In rectangular waveguides, at a given operating frequency of f, there is a propagation if the $f > f_{c_{mn}}$. So, In this project, the operating frequency range is from 10 GHz to 11.5 GHz, therefore TE_{10} is the only available mode of operation for our MRA.

Table 3.1: WR-90 waveguide transverse electromagnetic modes.

TE_{10}	6.56 GHz
TE_{01}	13.12 GHz
TE_{20}	13.13 GHz
TM_{11},TE_{11}	14.67 GHz
TE_{02}	26.25 GHz

3.3 Horn Antenna Field Patterns

The field pattern of the horn antenna is analytically calculated as follows. The parameters needed in the calculations are shown in Fig. 3.4.

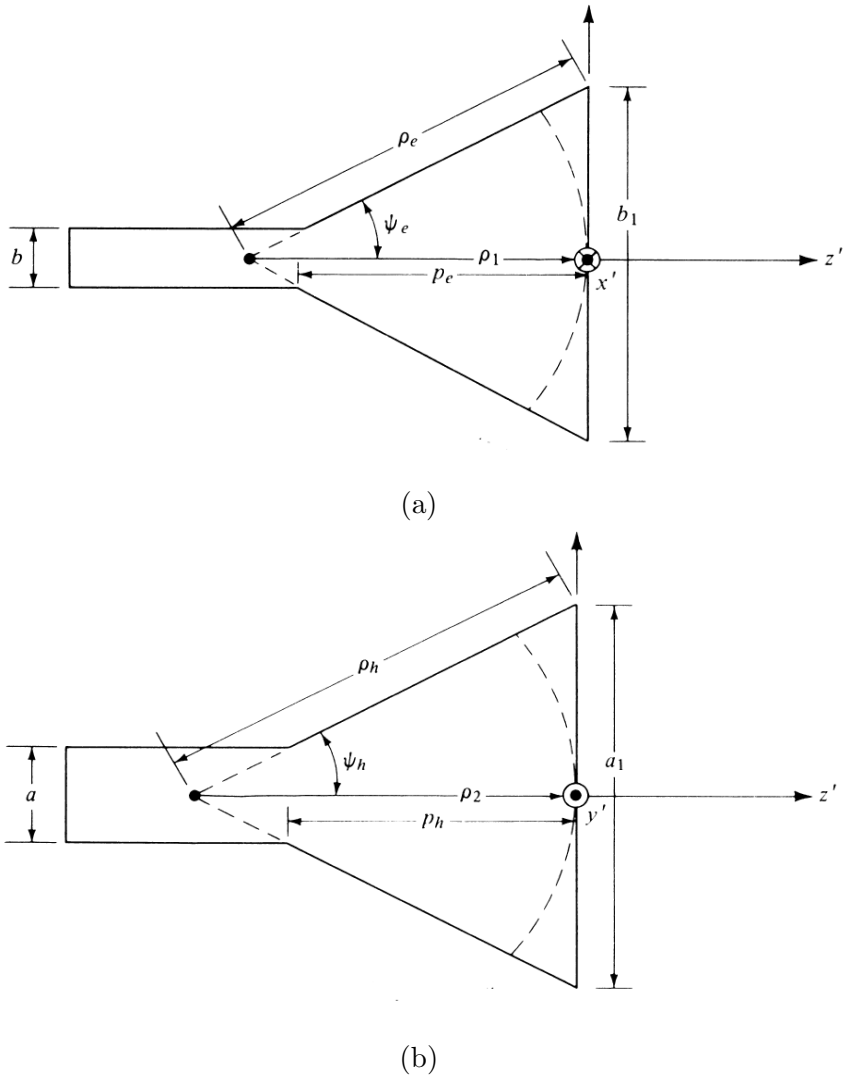

Fig. 3.4: (a)E-plane view (b)H-plane view of the pyramidal horn.

We know the dimensions of the horn antenna as in Fig. 3.2. Therefore we found the necessary parameters for the field pattern calculations as $a = 0.76\lambda$, $b = 0.34\lambda$, $a_1 = 1.33\lambda$, $b_1 = 0.97\lambda$, $\rho_1 = \rho_2 \approx 1.75\lambda$, where λ denotes wavelength in air at 10 GHz. and k is the

free space phase constant at the same frequency.

$$E_r = 0 \tag{3.2}$$

$$E_\theta = j\frac{kE_0e^{-jkr}}{4\pi r}[sin\phi(1+cos\theta)I_1I_2] \tag{3.3}$$

$$E_\phi = j\frac{kE_0e^{-jkr}}{4\pi r}[cos\phi(1+cos\theta)I_1I_2] \tag{3.4}$$

The field pattern of the pyramidal horn can be calculated with the equations (3.2-3.4). Where I_1 and I_2 can be expressed as [13]:

$$\begin{aligned} I_1 = \frac{1}{2}\sqrt{\frac{\pi\rho_2}{k}}(e^{jk_x^{'2}\rho_2/2k}\{[C(t_2^{'}) - C(t_1^{'})] - j[S(t_2^{'}) - S(t_1^{'})]\} \\ + e^{jk_x^{''2}\rho_2/2k}\{[C(t_2^{''}) - C(t_1^{''})] - j[S(t_2^{''}) - S(t_1^{''})]\}) \end{aligned} \tag{3.5}$$

$$I_2 = \sqrt{\frac{\pi\rho_1}{k}}e^{jk_y^2\rho_1/2k}\{[C(t_2) - C(t_1)] - j[S(t_2) - S(t_1)]\} \tag{3.6}$$

$$t_1 = \sqrt{\frac{1}{\pi k\rho_1}}(-\frac{kb_1}{2} - k_y\rho_1) \tag{3.7}$$

$$t_2 = \sqrt{\frac{1}{\pi k\rho_1}}(\frac{kb_1}{2} - k_y\rho_1) \tag{3.8}$$

$$t_1^{'} = \sqrt{\frac{1}{\pi k\rho_2}}(-\frac{ka_1}{2} - k_x^{'}\rho_2) \tag{3.9}$$

$$t_2^{'} = \sqrt{\frac{1}{\pi k\rho_2}}(\frac{ka_1}{2} - k_x^{'}\rho_2) \tag{3.10}$$

$$t_1^{''} = \sqrt{\frac{1}{\pi k\rho_2}}(-\frac{ka_1}{2} - k_x^{''}\rho_2) \tag{3.11}$$

$$t_2^{''} = \sqrt{\frac{1}{\pi k\rho_2}}(\frac{ka_1}{2} - k_x^{''}\rho_2) \tag{3.12}$$

$$k_x = ksin\theta cos\phi \tag{3.13}$$

$$k_y = ksin\theta cos\phi \tag{3.14}$$

$$k_x^{'} = ksin\theta cos\phi + \frac{\pi}{a_1} \tag{3.15}$$

$$k_x'' = ksin\theta cos\phi - \frac{\pi}{a_1} \tag{3.16}$$

$C(x)$ and $S(x)$ are Fresnel integrals, which are given as [13]:

$$C(x) = \int_0^x cos(t^2)dt = \sum_{n=0}^{\infty}(-1)^{-n}\frac{x^{4n+3}}{(2n+1)!(4n+3)} \tag{3.17}$$

$$S(x) = \int_0^x sin(t^2)dt = \sum_{n=0}^{\infty}(-1)^{-n}\frac{x^{4n+1}}{(2n)!(4n+1)} \tag{3.18}$$

The field patterns can also be obtained by full-wave simulations. It can be readily seen in Fig. 3.5 that the normalized field pattern obtained by the analytical method and full-wave simulation agree reasonably well.

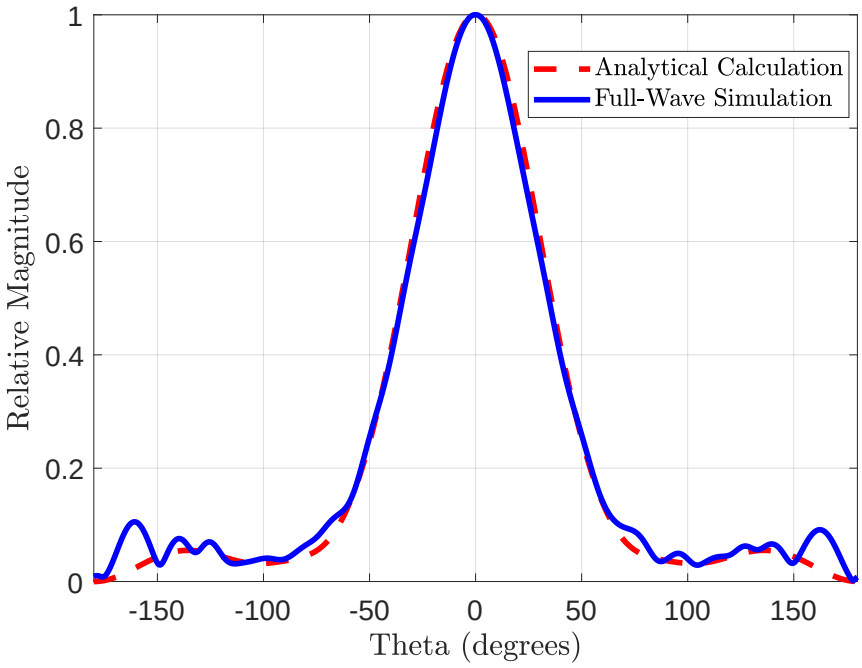

Fig. 3.5: Normalized field patterns obtained by the analytic method and full-wave simulation.

3.4 Directivity of Horn Antenna

The directivity of the pyramidal horn can be calculated with the given equations below [13]:

$$D_p = \frac{4\pi U_{max}}{P_{rad}} = \frac{8\pi\rho_1\rho_2}{a_1 b_1}\{[C(u)-C(v)]^2+[S(u)-S(v)]^2\} \times \{C^2(\frac{b_1}{\sqrt{2\lambda\rho_1}})+S^2(\frac{b_1}{\sqrt{2\lambda\rho_1}})\} \tag{3.19}$$

Where u and v are can be expressed as [13]:

$$u = \frac{1}{\sqrt{2}}(\frac{\sqrt{\lambda\rho_2}}{a_1}+\frac{a_1}{\sqrt{\lambda\rho_2}}) \tag{3.20}$$

$$u = \frac{1}{\sqrt{2}}(\frac{\sqrt{\lambda\rho_2}}{a_1}-\frac{a_1}{\sqrt{\lambda\rho_2}}) \tag{3.21}$$

Fig. 3.6 shows the horn directivity obtained by the analytic method and full-wave simulations. It can be seen that they both match with a slight difference in higher frequencies.

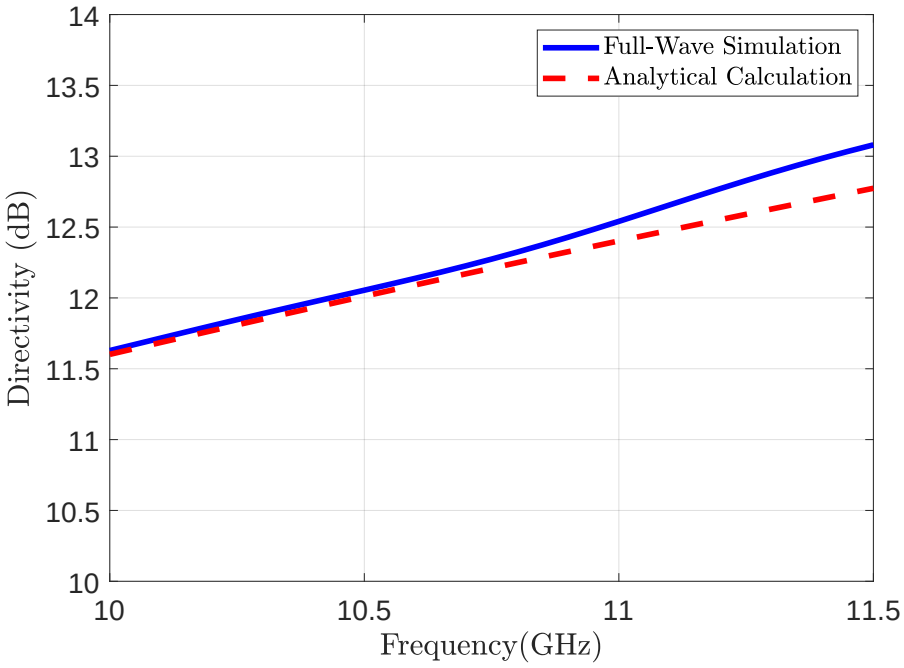

Fig. 3.6: Horn directivity obtained by the analytic method and full-wave simulation.

CHAPTER 4

Dielectric Loaded Truncated Pyramid Design

4.1 DLTP Architecture

After designing the horn antenna, the dielectric loaded truncated pyramid (DLTP) [4] is designed. DLTP is strategically located on top of the horn antenna, which is used to provide further gain enhancement and designed using Teflon PTFE ($\epsilon_r = 2.1, \tan\delta = 0.001$) [18]. DLTP has square shape base and the top. The geometry of a dielectric loaded truncated pyramid is shown in Fig. 4.1.

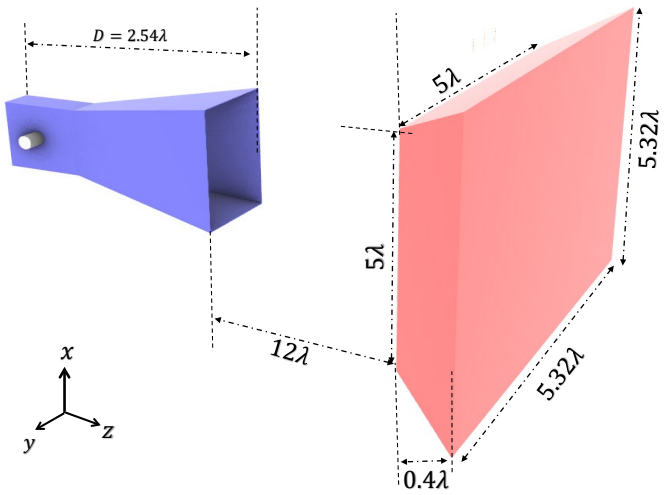

Fig. 4.1: The geometry of dielectric loaded truncated pyramid.

4.2 Shape Determination of the Dielectric Loaded Material Structure

DLTP is designed for the magnification purpose, and the shape of the truncated pyramid is also used in some studies [4]. DLTP works as a plano-convex lens. The shape of the truncated pyramid is chosen for two reasons. First, it provides almost the same performance in directivity compared to plano-convex shape lens, but it is easier to fabricate the structure

with sharp edges. Fig. 4.2 shows the shape effect on the directivity results. It can be seen from the results that the shape of the truncated pyramid and plano-convex provide similar magnification for the horn antenna.

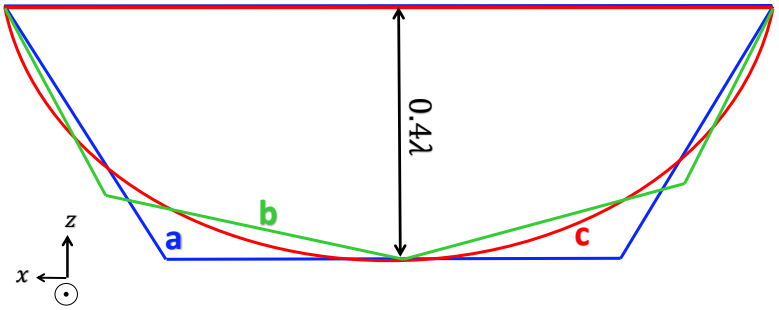

(a)

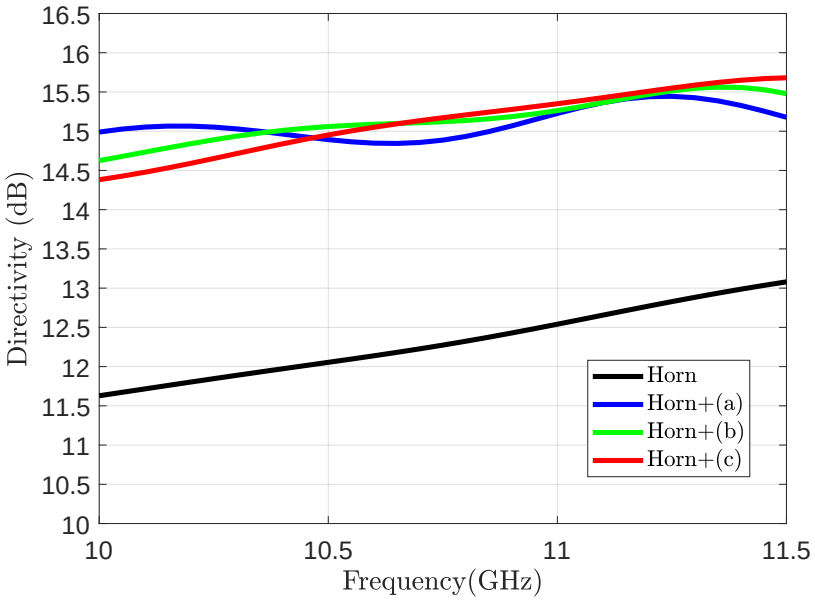

(b)

Fig. 4.2: (a) Shapes that are used for comparison and (b) related directivity results.

However, the thickness of the dielectric loaded structure plays a considerable role. The full-wave simulations are used to find the optimum thickness as 0.4λ. Fig. 4.3 shows the

effect of the thickness on the directivity results. When the design reaches the thickness of 0.4λ, it provides maximum directivity and magnification. Then, as we increase the thickness more, we see degradation in directivity results.

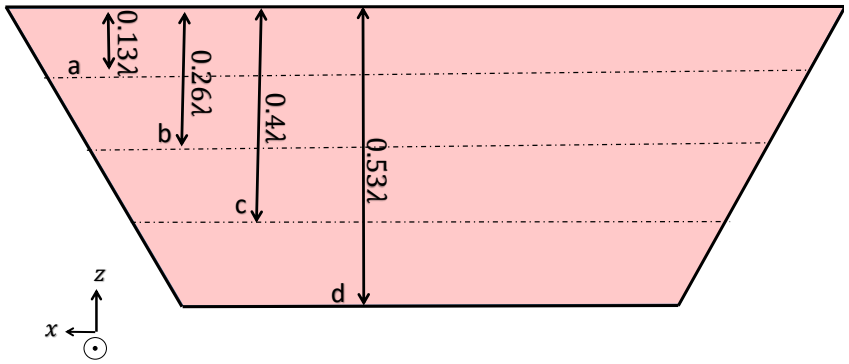

(a)

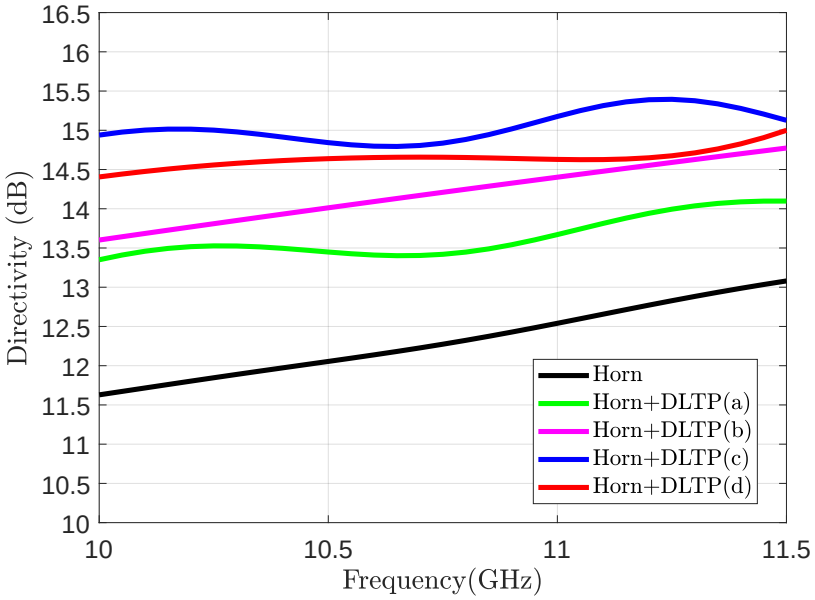

(b)

Fig. 4.3: (a) DLTP with different thicknesses and (b) related directivity results.

4.3 Working Mechanism of the DLTP

The working mechanism of the DLTP can be explained by the ray optics and lens

theory [19]. Dielectric lenses can transform spherical waves into planar waves, or they can focus plane waves [20]. Depending on the distance from the antenna, the waves can be approximated as spherical or planar, i.e., at the far field planar waves can be observed. The fields surrounding an antenna can be given as [13]:

$$\text{Far Field} \geq \frac{2D^2}{\lambda} \tag{4.1}$$

$$\text{Radiating Near Field} \leq \frac{2D^2}{\lambda} \tag{4.2}$$

$$\text{Reactive Near Field} \leq 0.62 \times \sqrt{\frac{D^3}{\lambda}} \tag{4.3}$$

In the given equations, D denotes the maximum dimension of the antenna, which is 2.54λ for the designed horn antenna. By using (4.1), the far field criteria for the horn antenna can be derived as $\sim 12\lambda$. Therefore, DLTP is located at the far field, and one can treat the bore side radiation of the horn antenna as a planar wave, as shown in Fig. 4.4.

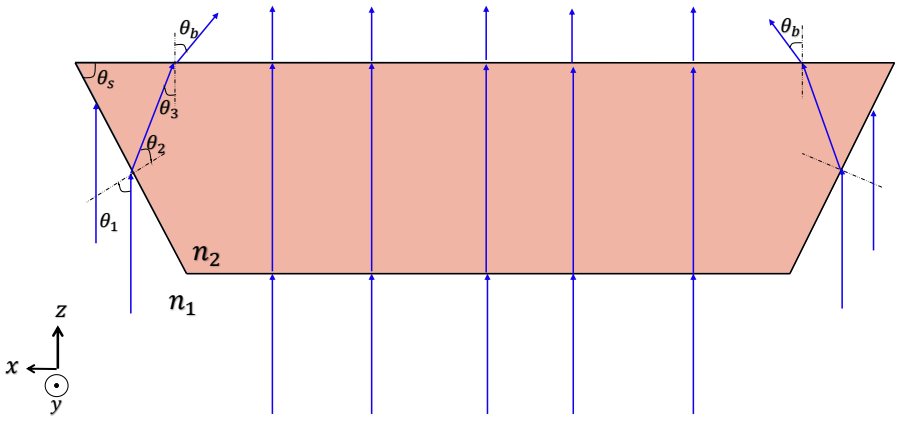

Fig. 4.4: Plane waves on DLTP.

During the dimension selection process, full-wave simulations and analytical calculations are used. The dimensions of the DLTP are chosen to provide focusing with an angle of θ_b as in Fig. 4.4. The base and top dimensions are selected as 5λ and 5.32λ as in Fig.

4.1. We also choose the material as Teflon, which can be easily fabricated and processed, and it has a low dielectric constant, which does not affect the reflection coefficient much. To find the direction of the planar waves at the boundaries, we used Snell's law [21]:

$$n_1 sin\theta_1 = n_2 sin\theta_2 \tag{4.4}$$

$$n_2 sin\theta_3 = n_1 sin\theta_b \tag{4.5}$$

From the geometry of the DLTP, θ_s can be found as 68.2°, which is the same as θ_1. The refractive index of the air is shown as n_1, and it is 1, while n_2 denotes the refractive index of Teflon, and it is 1.35. After calculating the angles by using the equations (4.4) and (4.5), θ_b is 34°.

To compare analytical calculations and full-wave simulations of the DLTP, we obtained directivity results in both ways. In analytical calculations, the radiated power needs to be calculated, which is an integration to the entire sphere as [13]:

$$D_0 = \frac{4\pi U_{max}}{P_{rad}} \tag{4.6}$$

$$U_{max} = B_0 F_{max}(\theta, \phi) \tag{4.7}$$

$$P_{rad} = \int_\Omega U(\theta, \phi)\, d\Omega = B_0 \int_0^{2\pi} \int_0^{\pi} F(\theta, \phi) sin\theta d\theta d\phi \tag{4.8}$$

$$D_0 = 4\pi \frac{F_{max}(\theta, \phi)}{\int_0^{2\pi} \int_0^{\pi} F(\theta, \phi) sin\theta d\theta d\phi} \tag{4.9}$$

However, for a directive antenna, we only need to integrate over the main beam, which is the first null beamwidth (FNBW) [13]:

$$D_{Horn} = 2 \frac{F_{max}(\theta, \phi)}{\int_0^{FNBW/2} F(\theta, \phi) sin\theta d\theta} \tag{4.10}$$

After attaching the DLTP on top of the horn antenna, the more directive beam pattern is achieved as explained above. Therefore, we achieve a beam pattern, which has less FNBW

[22]. The lens bent the plane wave to an angle of θ_b. So, in the directivity calculations, we integrate for the main beam after focusing, which is the $FNBW - 2\theta_b$ [22]. The directivity after we attach the lens can be expressed as [13]:

$$D_{Horn+DLTP} = 2\frac{F_{max}(\theta,\phi)}{\int_0^{(FNBW-2\theta_b)/2} F(\theta,\phi)sin\theta d\theta} \tag{4.11}$$

4.4 DLTP Results

After calculating the equations (4.10) and (4.11), we found D_{Horn} as $\sim$ 11 dB and $D_{Horn+DLTP}$ as $\sim$ 15 dB. Thereby, analytical calculations show that DLTP can enhance the horn directivity by 4 dB. We also performed the full-wave simulations to show the change in the directivity and the FNBW as can be seen in Fig. 4.5.

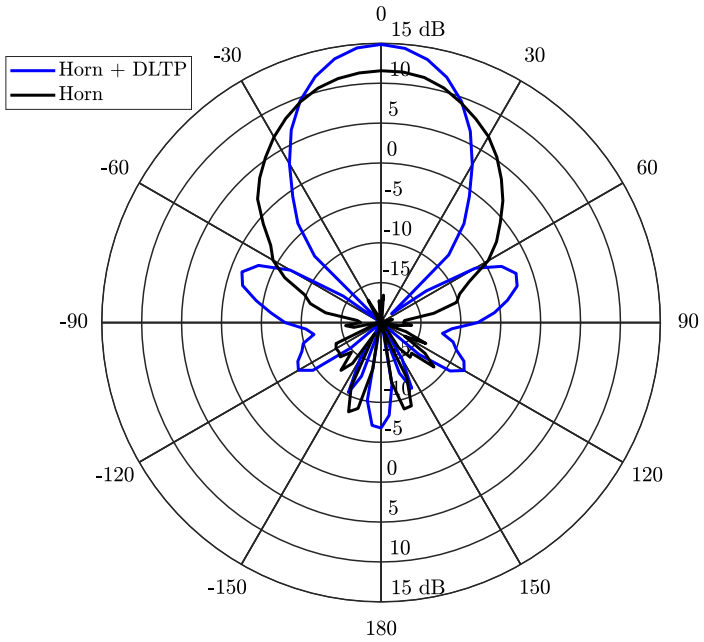

Fig. 4.5: Directivity results from the full-wave simulations.

We can see that analytical calculations and the full wave simulations agree well. They both show the enhancement in the directivity around 4 dB. Also, it can be seen that the difference in FNBW is around 72°, which is close to our approximation.

CHAPTER 5

Parasitic Pixel Layer Design

5.1 Parasitic Layer Architecture

Next, the parasitic layer for the radiation pattern reconfiguration is designed. The parasitic layer is designed independently from DLTP, and the overall optimization is done in the combination part where we put all the MRA components together. The overall structure of the designed parasitic layer is shown in Fig. 5.1. The parasitic layer is built using the Rogers 4003C ($\epsilon_r = 3.55, \tan\delta = 0.0027$) substrate [23]. The top surface of this layer consists of 4x4 square metallic pixels ($0.13\lambda \times 0.13\lambda$) which are interconnected by PIN diode switches. The bias lines through which the PIN diode switches are controlled are located on the top surface of the parasitic layer. To provide biasing, thru-hole vias that are running from the top to the bottom surface of the parasitic layer are also used around the grounding inductor connections.

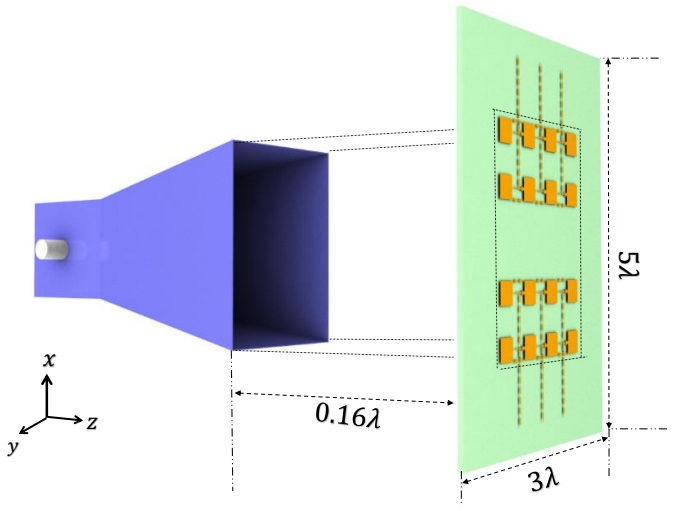

Fig. 5.1: The geometry of the parasitic layer together with horn antenna.

The main design parameters of the parasitic layer are the pixel length, width, separation between adjacent pixels, and parasitic layer thickness. The pixel dimensions are designed to enhance beam steering by maximizing the coupling with the horn antenna. The distance between the parasitic layer and the driven antenna strongly affects their mutual coupling [2]. In the presented MRA, a driven horn antenna is mutually coupled with four reconfigurable pixelated parasitic strips that are placed above the driven element, with vertical distance between driven antenna layer and parasitic layer being 0.16λ. Therefore, at the height where the steering is maximized, the number of pixels, their separation and their distribution on the reconfigurable parasitic surface are determined to yield proper impedance matching. Once the pixel layer has been optimized, the biasing circuitry through which the PIN diodes are controlled is obtained. To this end, the locations and positions are determined to place the PIN diodes, RF chokes, DC grounding inductors, and DC blocking capacitors, as shown in Fig. 5.2.

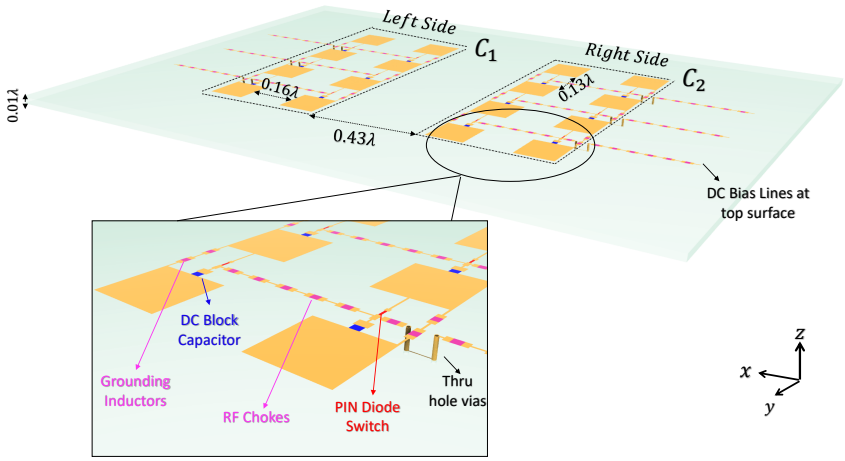

Fig. 5.2: Magnified view of the parasitic layer.

MRA horn is aimed to steer its main beam in three directions in the semi-sphere space of $\theta \in \{-25^o, 0^o, 25^o\}$. Table 5.1 shows the modes, beam steering angles, and associated switch configurations.

Table 5.1: Switch configuration for three modes of operations.

Modes	θ	ϕ	Left Switches	Right Switches
0	0^o	0^o	OFF	OFF
1	25^o	0^o	OFF	ON
2	-25^o	0^o	ON	OFF

5.2 Working Mechanism of the Parasitic Layer

The working mechanism of the parasitic layer can be explained by the phased array principle where the beam steering is achieved by the phase difference of the array elements. The effective electrical lengths of the parasitic strip elements are changed by switching ON/OFF the interconnecting PIN diodes, to achieve phase difference at the sides. This phase difference causes the main beam of the MRA to be steered away from its broadside direction. As depicted in Fig. 5.2, when the right side switches are turned ON, left side switches are turned OFF, the effective electrical length of the right side becomes larger and left side becomes smaller, which creates the phase difference and hence beam steering.

Fig. 5.2 shows the switch sides and closed loops over the parasitic elements that are used for analytical calculations. Since, we turn ON or OFF all the switches together at one side, for the ease of analysis, we approximated the pixels as microstrips at each side and solved by using 1x2 linear microstrip array as it can be seen in Fig. 5.3.

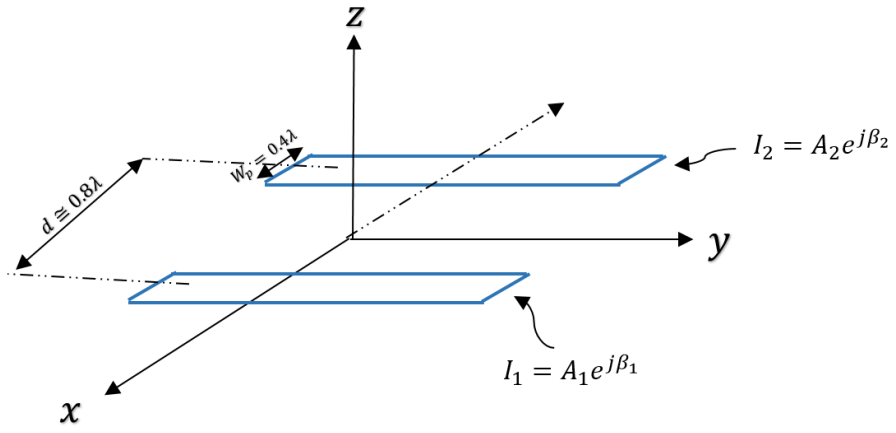

Fig. 5.3: 1x2 Microstrip array approximation for ease of analysis.

$$I_n = \oint_{C_n} H \cdot dl \tag{5.1}$$

$$I = \begin{cases} I_1 \approx 0.12e^{j2.12}; I_2 \approx 0.12e^{j3.83} & \text{for Mode 1} \\ I_1 \approx 0.12e^{j2.12}; I_2 \approx 0.12e^{j2.12} & \text{for Mode 0} \\ I_1 \approx 0.12e^{j3.83}; I_2 \approx 0.12e^{j2.12} & \text{for Mode 2} \end{cases} \tag{5.2}$$

The complex currents I_1, I_2 are calculated by using the equation (5.1), which does the integration of magnetic fields H_1, H_2 along the closed curves C_1 and C_2, as shown in Fig. 5.2 [9]. Calculated current values for obtaining the radiation patterns for each mode of operations are given in (5.2).

$$I_1 = A_1 e^{j\beta_1}; I_2 = A_2 e^{j\beta_2}; \beta = \beta_1 - \beta_2 \tag{5.3}$$

$$\theta = \arcsin(-\frac{\beta}{kd}) \tag{5.4}$$

$$\theta = \begin{cases} \theta \approx 23^\circ & \text{for Mode 1} \\ \theta \approx 0^\circ & \text{for Mode 0} \\ \theta \approx -23^\circ & \text{for Mode 2} \end{cases} \tag{5.5}$$

By using equation (5.3), the phase difference of the array elements can be calculated. The maximum of the array factor direction equation is given in (5.4). Also, notice that the array axis, on which the centers of the elements are placed, is the x-axis. So, we used the array formulas accordingly. Obtained array factor direction results for each mode of operation are given in (5.5).

$$\psi = kdsin\theta cos\phi + \beta \tag{5.6}$$

$$\text{Array Factor} = \frac{1}{N}\frac{sin(\frac{N\psi}{2})}{sin(\frac{\psi}{2})} \tag{5.7}$$

$$\text{Element Factor} = cos\theta \frac{sin(\frac{kW_p}{2}sin\theta)}{\frac{kW_p}{2}sin\theta} \tag{5.8}$$

5.3 Parasitic Layer Results

To be able to compare analytical calculations with full-wave simulations, the field patterns are calculated by using given equations (5.6-5.8) [9]. Where N is the number of the array element, d is the interelement distance, and W_p is the approximated microstrip width, as shown in Fig. 5.3. The normalized field patterns for each mode obtained by full-wave simulation and analytical method are given in Fig. 5.4. The results indicate that analytical calculations and full-wave simulations agree for all modes.

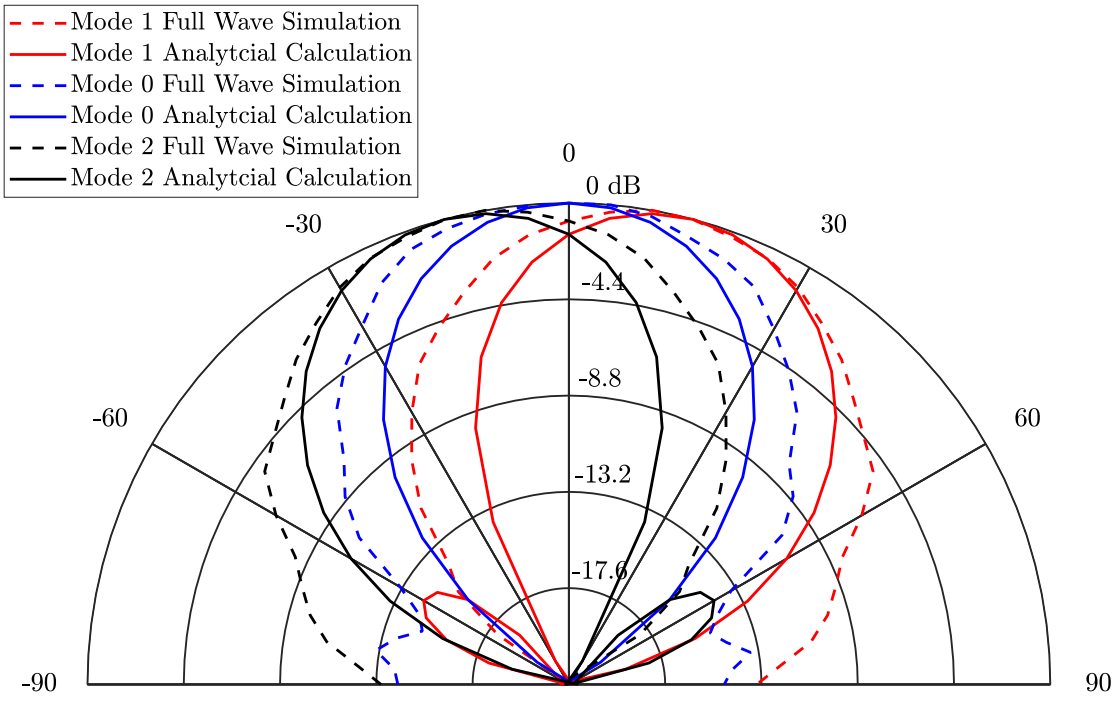

Fig. 5.4: Normalized field patterns for each mode obtained by full-wave simulation and the analytical method.

CHAPTER 6

Overall MRA Combination and Optimization

6.1 Overall MRA Architecture

After designing the parasitic layer, all the designed components are combined and optimized to create a radiation pattern reconfigurable horn antenna. The overall structure of the designed overall MRA is shown in Fig. 6.1.

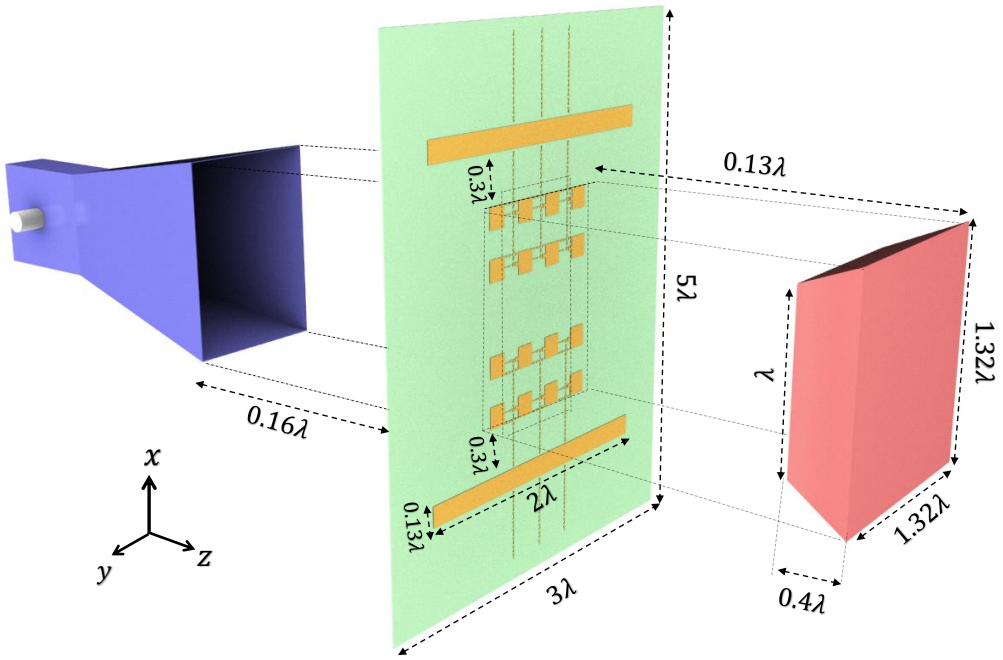

Fig. 6.1: 3D exploited view of overall MRA.

The main two components of the MRA architecture are DLTP and reconfigurable parasitic layer. Driven horn antenna is designed to operate at X-band (10 GHz - 11.5 GHz). The parasitic layer is built using the Rogers 4003C ($\epsilon_r = 3.55, \tan\delta = 0.0027$) substrate [23]. The top surface of this layer consists of 4x4 square metallic pixels which are interconnected

by PIN diode switches. This surface also accommodates two rectangular strips, which are used for gain enhancement. The bias lines through which the PIN diode switches are controlled are located on the top surface of the parasitic layer. DLTP is strategically located on top of the parasitic layer, which is used to provide further directivity enhancement and designed using Teflon material ($\epsilon_r = 2.1, \tan\delta = 0.001$).

6.2 Optimization

6.2.1 DLTP Optimization

Before starting combining all MRA parts, DLTP is optimized with the smaller and closer one as given in Fig. 6.2. Optimization is done without putting the parasitic layer to see the DLTP still works. The directivity results are given in Fig. 6.3.

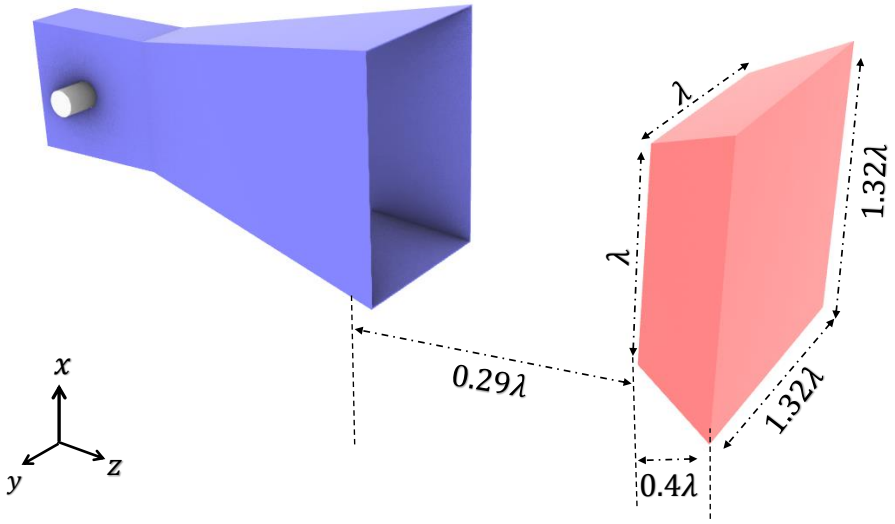

Fig. 6.2: The geometry of the optimized dielectric loaded truncated pyramid.

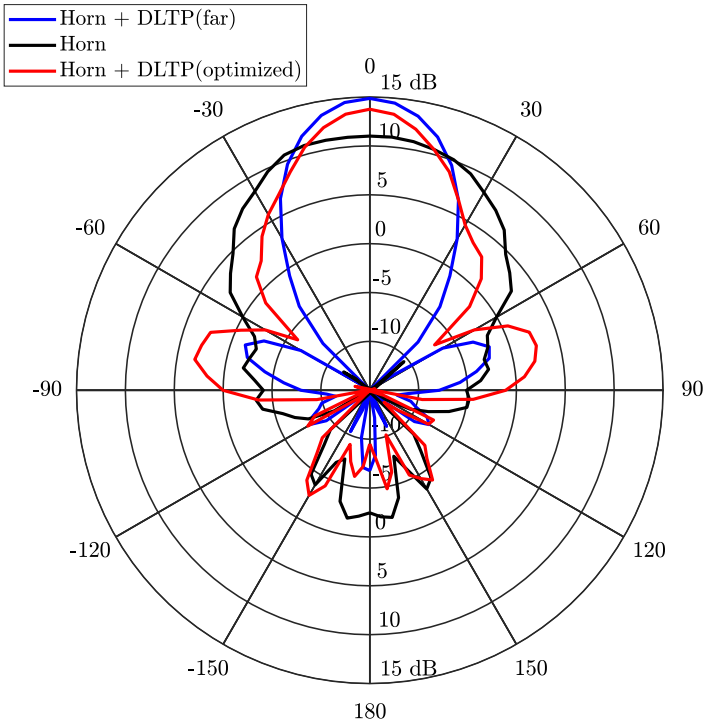

Fig. 6.3: Directivity results obtained by full-wave simulation after DLTP optimization.

It can be seen in Fig. 6.3 that there is a drop in directivity ~ 1 dB compared with the previous DLTP. It is because the incoming electromagnetic waves from the horn antenna to the DLTP are no longer as planar as it was before. Even with a drop in directivity results, the design is smaller and compact. Also, the holder mechanisms for the DLTP and parasitic layer have less impact on overall performance for the practical design, and the cost for the fabrication is reduced. Also, the mobility of the MRA is improved.

$$I = \begin{cases} I_1 \approx 0.15e^{j2.25}; I_2 \approx 0.15e^{j3.98} & \text{for Mode 1} \\ I_1 \approx 0.15e^{j2.25}; I_2 \approx 0.15e^{j2.25} & \text{for Mode 0} \\ I_1 \approx 0.15e^{j3.98}; I_2 \approx 0.15e^{j2.25} & \text{for Mode 2} \end{cases} \tag{6.1}$$

After optimizing the DLTP, we put the parasitic layer in between horn and optimized DLTP as in Fig. 6.1, where the driven horn antenna is mutually coupled with the parasitic

layer at the height where the beam steering is maximized with the vertical distance between the driven antenna and parasitic layer being 0.16λ. The complex currents on the parasitic layer I_1, I_2 are calculated again to make sure the phase difference is still there to achieve beam steering. By using equation (5.1), magnetic fields H_1, H_2 are again calculated along the closed curves C_1 and C_2 as shown in Fig. 5.2 [9]. After combining all MRA components, calculated current values for obtaining the radiation patterns for each mode of operations are given in (6.1).

$$\theta = \begin{cases} \theta \approx 23^\circ & \text{for Mode 1} \\ \theta \approx 0^\circ & \text{for Mode 0} \\ \theta \approx -23^\circ & \text{for Mode 2} \end{cases} \tag{6.2}$$

For all modes, the maximum of array factor directions after combining all MRA components are given in (6.2). The results show that the beam steering still can be achieved. Therefore, the height of the parasitic layer is fixed to provide beam steering. Also, by optimizing the DLTP at the beginning, we are able to provide magnification for all modes; otherwise DLTP was providing magnification for Mode 0 only. The vertical distance between the parasitic layer and DLTP is optimized to get maximum magnification, which is found as 0.13λ as shown in Fig. 6.1. The beam steering and the magnification of the radiation patterns after we attach the DLTP for each mode of operations are shown in Fig. 6.4.

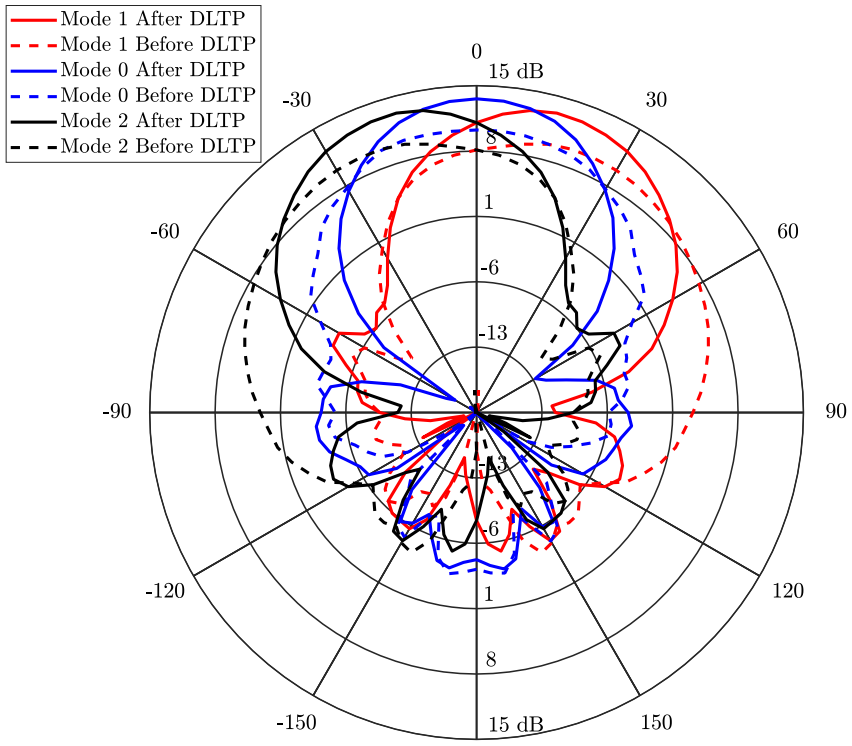

Fig. 6.4: Directivity comparison all modes.

6.2.2 Adding Two Strips

Furthermore, to increase the directivity, we designed two strips on the parasitic layer, as shown in Fig. 6.1 which squeezes the beam pattern. They are able to enhance the directivity around $\sim$ 0.35 dB for all modes. The working mechanism of these two strips can be explained by 1x2 microstrip arrays which are excited with currents that have the same amplitude and phase, which leads to more directive pattern. The simulated directivity results that show for all modes with respect to frequency are given in Fig. 6.5.

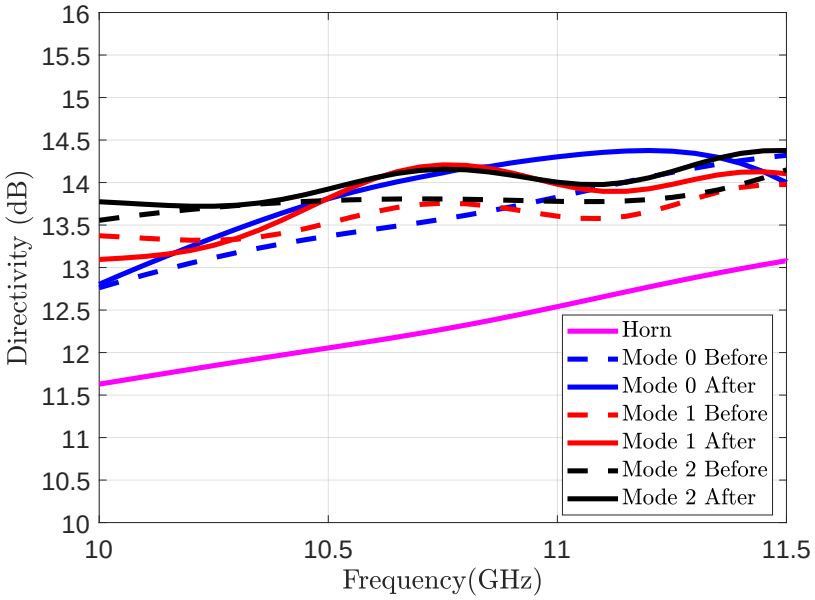

Fig. 6.5: Directivity enhancement of all modes by two strips.

6.3 Overall MRA Results

In this section, the directivity, radiation patterns, and reflection coefficients results for the designed MRA are presented. Fig. 6.6 shows the directivity results for each mode of operations. The results for horn antenna are also given as a reference. As can be seen, MRA provides significant directivity enhancement in all directions. The simulated reflection coefficient results for all modes with respect to frequency are given in Fig. 6.7. Also, simulated directivity results for all modes with respect to frequency are given in Fig. 6.8. It can be seen that directivity stays relatively stable over the whole frequency band. At the end, the simulated radiation efficiency results for all modes with respect to frequency are given in Fig. 6.9. It can be seen that the efficiency results of the modes are still high enough, and the directivity results are close to realized gain values.

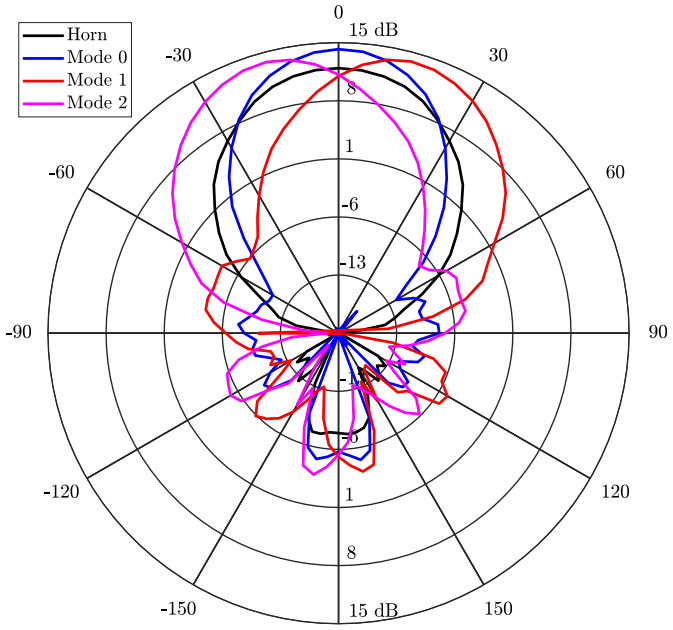

Fig. 6.6: Simulated directivity patterns at 10.7 GHz.

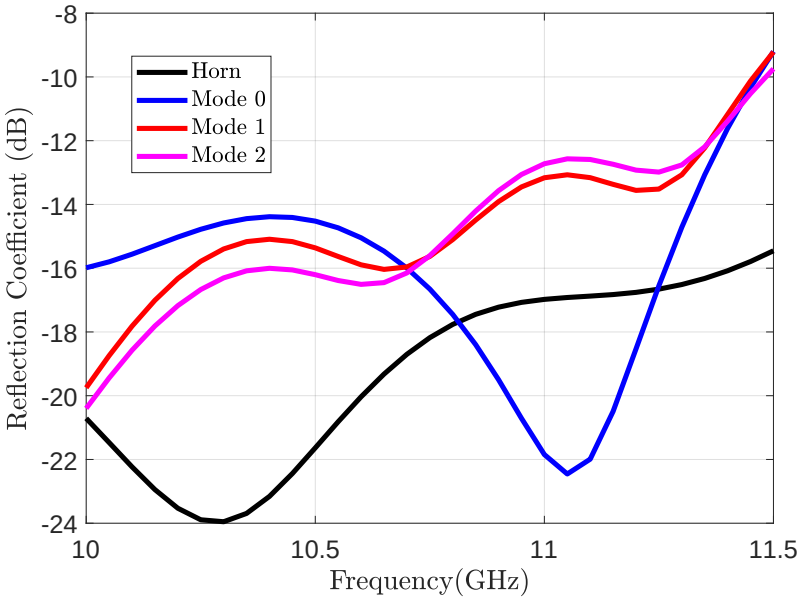

Fig. 6.7: Simulated reflection coefficient results for all modes with respect to frequency.

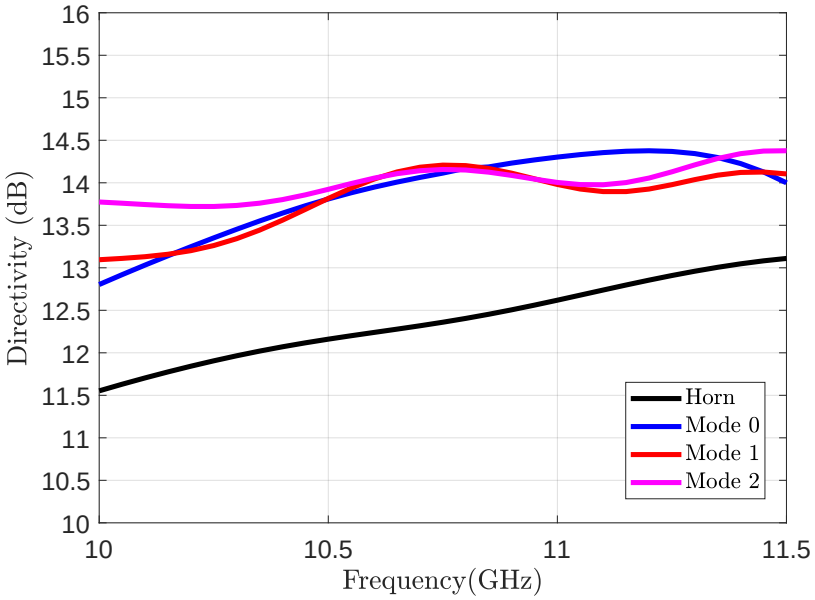

Fig. 6.8: Simulated directivity results for all modes with respect to frequency.

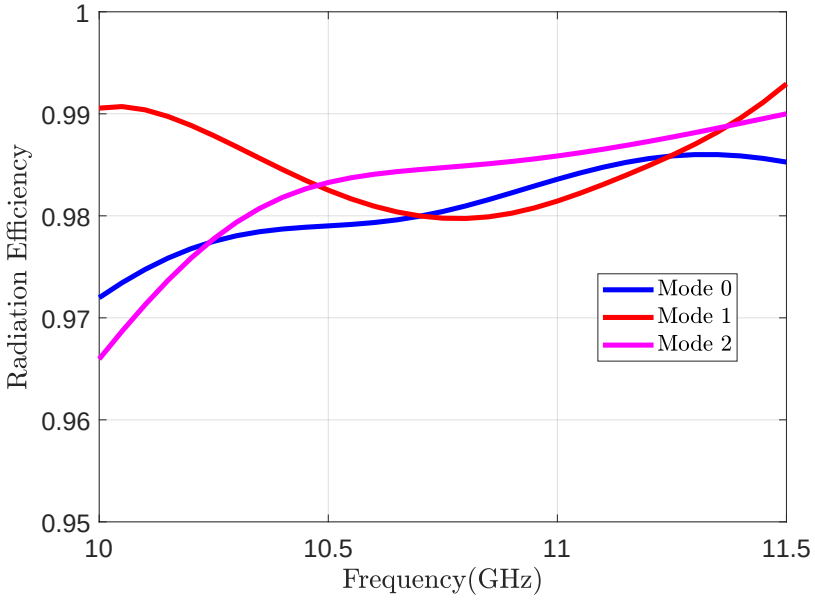

Fig. 6.9: Simulated radiation efficiency results for all modes with respect to frequency.

CHAPTER 7

Fabrication Guide

This chapter shows the necessary materials, steps, and methods to assemble and fabricate the MRA horn antenna. Fabrication has four stages, which are horn selection, DLTP fabrication, parasitic layer fabrication, and holder fabrication. In each section, the company that can get that part done is given. I have contacted all the mentioned companies and get their assessment to get the related part done.

7.1 Horn Antenna Selection

For the MRA, the horn antenna is WR-90 waveguide horn antenna operating from 8.2 GHz to 12.4 GHz with a nominal 10 dB gain, which can be purchased from Pasternack [15].

7.2 DLTP Fabrication

The DLTP structure is made of Teflon PTFE ($\epsilon_r = 2.1, \tan\delta = 0.001$) [18] and is given in Fig. 7.1. DLTP structure needs a thin layer with a thickness of 0.025λ on the top, which is designed for holding purpose, as shown in Fig. 7.1. PTFE is easily machined and is also used for precision and intricate parts. The material, Teflon (PTFE), can be milled with resources such as Chicago Plastic Systems (CPS) [24]. The dimensions and the drawings of the DLTP are sent to the CPS and confirmed via e-mail that they are able to manufacture the DLTP structure.

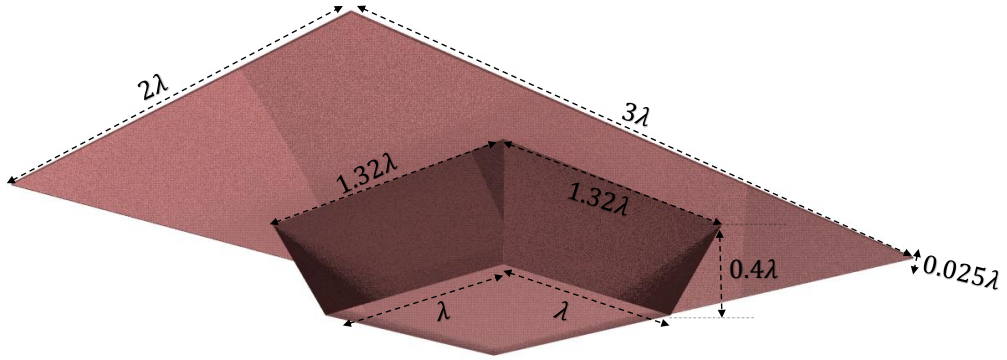

Fig. 7.1: 3D view of the DLTP (λ denotes wavelength in air at 10 GHz).

7.3 Parasitic Layer Fabrication

The board design can be completed by using one of the PCB design application such as Altium Designer [25], then the design can be sent to be fabricated to the resource such as Quick Turn Circuits (QTC) [26]. The material for the pixels will be copper, and the thru holes on the biasing lines are plated, as shown in Fig. 7.2. There are also four non-plated holes at the corners which are aligned with the holes on the holder to hold the parasitic layer by using plastic screws. The parasitic layer is built using the Rogers 4003C ($\epsilon_r = 3.55, \tan\delta = 0.0027$) substrate with 0.01λ(0.3mm) thickness [23]. QTC company has confirmed that they can produce this design, including the plated and non-plated vias but will require the customer to ship Rogers substrate to them.

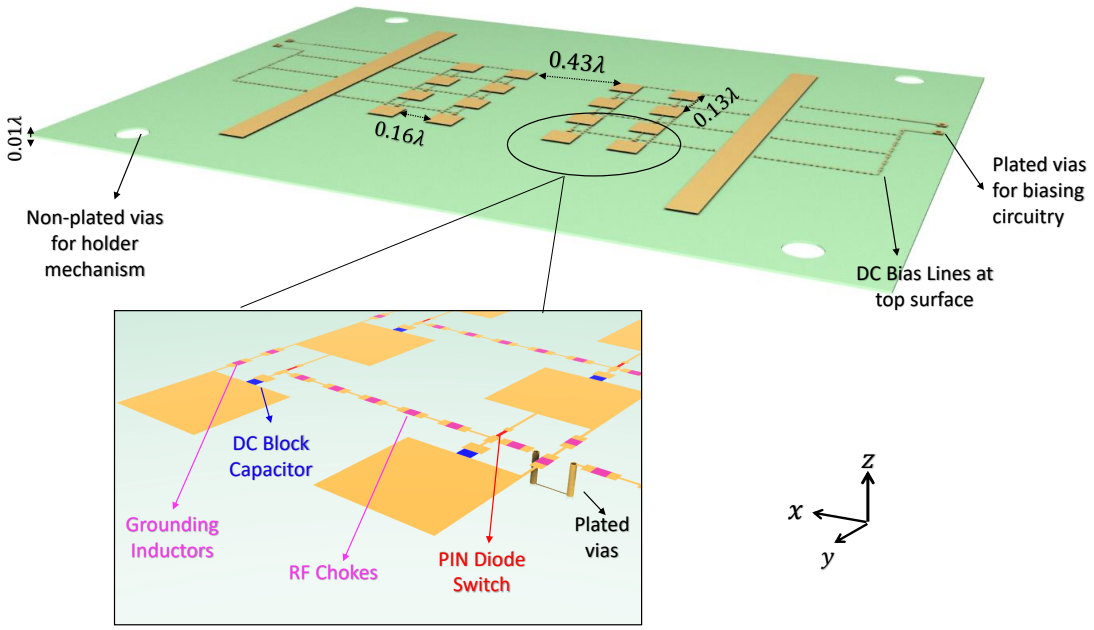

Fig. 7.2: Magnified view of the parasitic layer and used lumped components (λ denotes wavelength in air at 10 GHz).

After receiving the fabricated parasitic layer, the surface mount devices (SMD) can be placed. The manufacturers, values, and self-resonant frequencies (SRFs) of the SMDs on the parasitic layer are given in Table 7.1. Metal pad dimensions and the data-sheets of the SMD components are shared with Space Dynamics Laboratory (SDL) [27], and it is verified that they are able to place the SMD components on the parasitic layer.

7.4 Biasing Circuitry

Next, the biasing circuitry needs to be prepared. Fig. 7.3 shows the designed DC biasing scheme of the PIN diodes. Since the PIN diodes on the same side are enabled at the same time, the biasing scheme of one side has been shown. The manufacturers and values of the components that are needed to prepare the DC biasing circuit are given in Table 7.2.

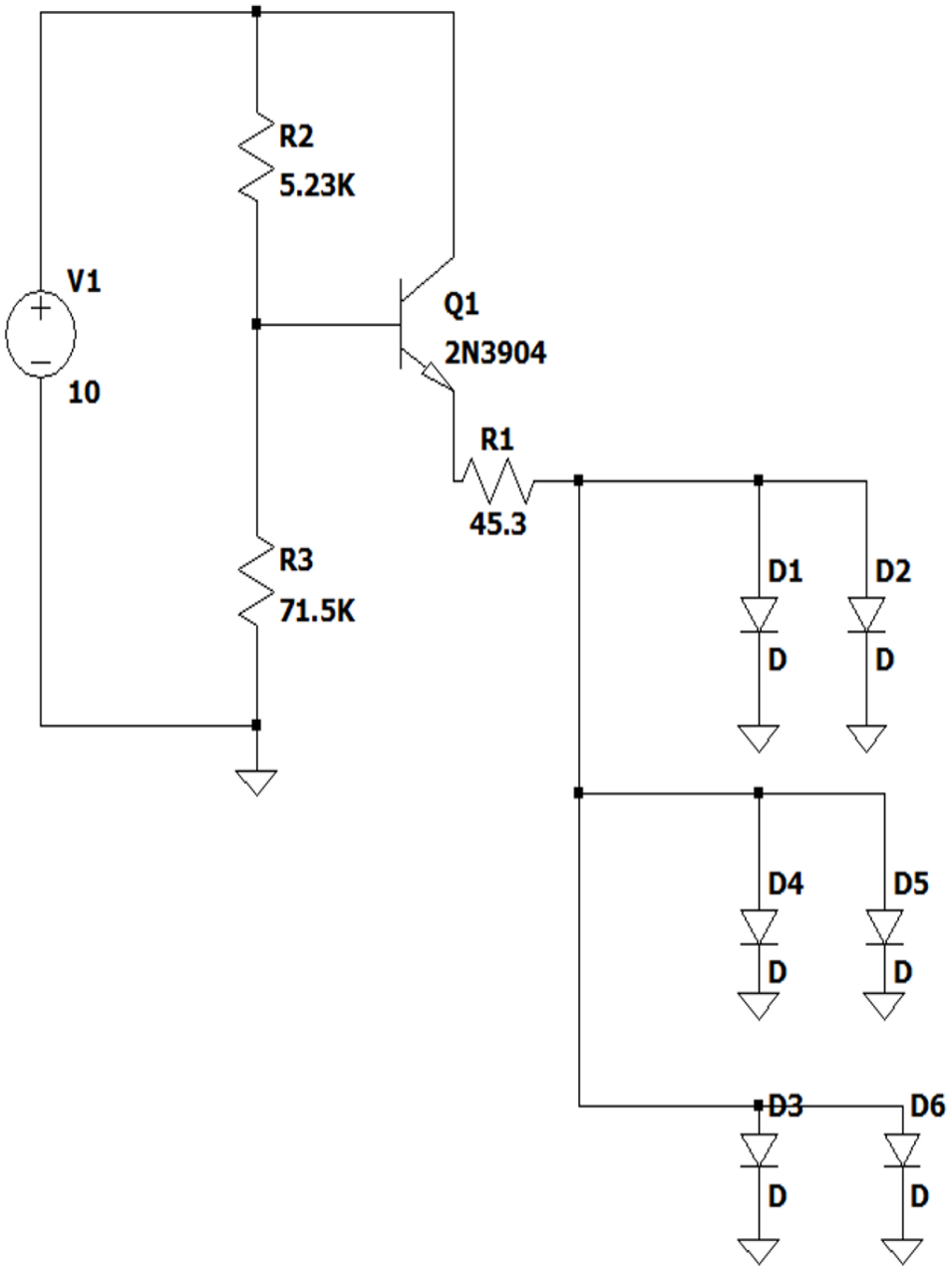

Fig. 7.3: DC biasing scheme of the PIN diodes.

Table 7.1: List of SMDs on the parasitic layer.

Manufacturer	Type	Value	SRF
Skyworks - DSG9500	PIN Diode Switch	N/A	N/A
Yuden - HKQ0603U1N5B	RF choke and DC grounding inductor	1.5 nH	10 GHz
ATC - 530L	DC Block capacitor	100 nF	10 GHz
2N3904	Bipolar Junction Tran - sistor	N/A	N/A
N/A	Resistor (R_1)	45.3 Ω	N/A
N/A	Resistor (R_2)	5.23 $k\Omega$	N/A
N/A	Resistor (R_3)	71.5 $k\Omega$	N/A

Table 7.2: Component list for power supply interface.

Manufacturer Part Number	Type	Quantity
TW-E40-510	Breadboard	2
PPPC021LFBN-RC	2 Position Header Connector 0.100” (2.54mm) Through Hole Gold	2
FSP-22A-2	2 Position Flexstrip Cable 0.100” (2.54mm) 2.000” (50.80mm)	2

7.5 Holder

The holder needs to be manufactured to hold both the truncated pyramid and the parasitic surface at the desired height as can be seen in Fig. 7.4. For the holder structure, 3D-printer [28] can be used. Material for the holder is chosen as ABS plus [28]. Also, notice that the surface on top of DLTP is enlarged with a thin layer to mount pyramid to holder

mechanism as shown in DLTP section.

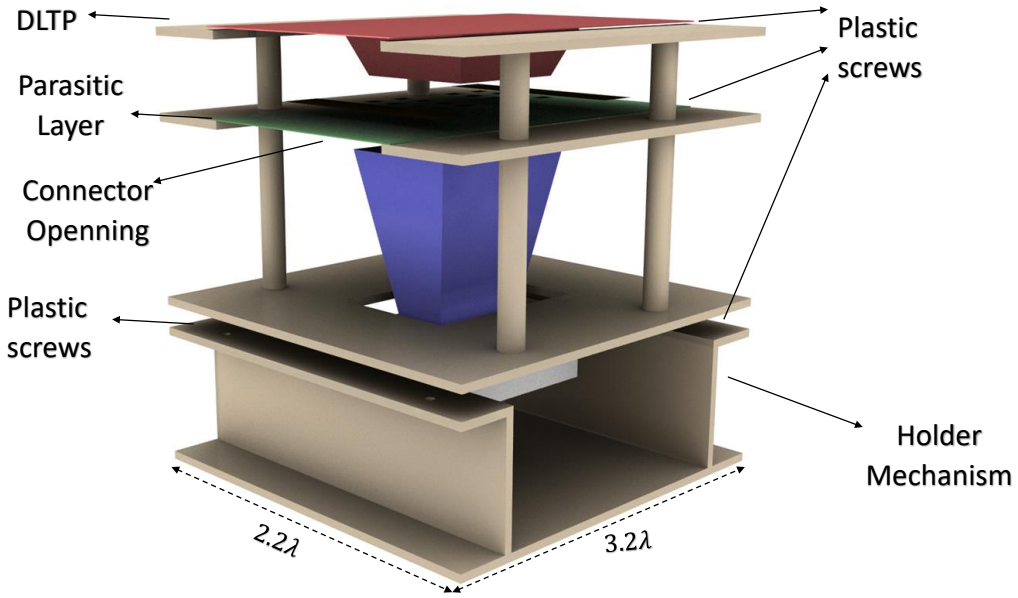

Fig. 7.4: Holder Mechanism (λ denotes wavelength in air at 10 GHz).

CHAPTER 8

Conclusion and Future Work

This thesis presented a model of the multifunctional reconfigurable antenna with the primary goal of providing radiation pattern reconfigurability for high gain horn antenna. The MRA is formed by a single horn antenna, parasitic layer, and dielectric material loaded truncated pyramid. MRA is capable of steering its main beam in three directions in the semi-sphere space corresponding to $\theta \in \{-25^o, 0^o, 25^o\}$ by reconfiguring the geometry of the parasitic pixel surface. This surface accommodates metallic pixels, and the geometry of this surface can be changed by switching ON/OFF the PIN diode switches between adjacent pixels. DLTP is used in the MRA to provide significant improvements to the performance. Electromagnetic (EM) full-wave analysis and analytical calculations are used for the design process. The results indicate that from 10 GHz to 11.5 GHz, a directivity of $\sim$ 14 dB is achieved in all modes of operation.

The future work will focus on the fabrication and characterization of the designed MRA with the provided fabrication guide. Then, the know-how, skills, and experience gained during the MRA Horn project will be used to design an MRA Array Horn (MRAA Horn). The ultimate MRAA will be 4x4 planar array, operating in the 40 GHz mm-wave band. At first, 1x4 linear MRAA Horn will be studied, which will then be expanded into 4x4 array. The full-wave EM design efforts will also take into account 3D air-metal-dielectric fabrication aspect of the MRAA Horn. The outcomes of this research are anticipated to yield significant results for antenna array theory in general.

REFERENCES

[1] X. Yuan, Z. Li, D. Rodrigo, H. S. Mopidevi, O. Kaynar, L. Jofre, and B. A. Cetiner, "A parasitic layer-based reconfigurable antenna design by multi-objective optimization," *IEEE Transactions on Antennas and Propagation*, vol. 60, no. 6, pp. 2690–2701, June 2012.

[2] D. Rodrigo, B. A. Cetiner, and L. Jofre, "Frequency, radiation pattern and polarization reconfigurable antenna using a parasitic pixel layer," *IEEE Transactions on Antennas and Propagation*, vol. 62, no. 6, pp. 3422–3427, June 2014.

[3] B. A. Cetiner, H. Jafarkhani, J.-Y. Qian, H. J. Yoo, A. Grau, and F. D. Flaviis, "Multifunctional reconfigurable mems integrated antennas for adaptive mimo systems," *IEEE Communications Magazine*, vol. 42, no. 12, pp. 62–70, Dec 2004.

[4] A. S. Turk and A. K. Keskin, "Partially dielectric-loaded ridged horn antenna design for ultrawideband gain and radiation performance enhancement," *IEEE Antennas and Wireless Propagation Letters*, vol. 11, pp. 921–924, 2012.

[5] D. Rodrigo, J. Romeu, B. A. Cetiner, and L. Jofre, "Pixel reconfigurable antennas: Towards low-complexity full reconfiguration," in *2016 10th European Conference on Antennas and Propagation (EuCAP)*, April 2016, pp. 1–5.

[6] O. Barro, M. Himdi, and A. Martin, "Electrically reconfigurable radiation patterns of slot antenna array using agile plasma wall," *Progress In Electromagnetics Research C*, vol. 73, 01 2017.

[7] A. Martin, V. Le Neillon, A. Jouade, and M. Himdi, "Mechanically reconfigurable radiation pattern slot antenna array feeded by bended sectoral horn and metalized wood splitter," vol. 72, pp. 159–165, 01 2017.

[8] D. Rodrigo, Y. Damgaci, M. Unlu, B. A. Cetiner, J. Romeu, and L. Jofre, "Antenna reconfigurability based on a novel parasitic pixel layer," in *Proceedings of the 5th European Conference on Antennas and Propagation (EUCAP)*, April 2011, pp. 3497–3500.

[9] M. A. Towfiq, I. Bahceci, S. Blanch, J. Romeu, L. Jofre, and B. A. Cetiner, "A reconfigurable antenna with beam steering and beamwidth variability for wireless communications," *IEEE Transactions on Antennas and Propagation*, vol. 66, no. 10, pp. 5052–5063, Oct 2018.

[10] M. A. Hossain, I. Bahceci, and B. A. Cetiner, "Parasitic layer-based radiation pattern reconfigurable antenna for 5g communications," *IEEE Transactions on Antennas and Propagation*, vol. 65, no. 12, pp. 6444–6452, Dec 2017.

[11] G. V. Trentini, "Partially reflecting sheet arrays," *IRE Transactions on Antennas and Propagation*, vol. 4, no. 4, pp. 666–671, October 1956.

[12] HFSS, "Ansoft corp., pittsburgh, pa," 2015.

[13] C. A. Balanis, *Antenna theory: Analysis and design.* John Wiley Sons, Inc., 2005.

[14] R. S. Piske, D. Rathod, and Y. Gothe, "Design and analysis of h plane horn antenna at x band frequency," *International Journal for Scientific Research and Development*, vol. 3, no. 04, pp. 2321–0613, 2015.

[15] *WR-90 Waveguide Standart Gain Horn Antenna Operating From 8.2 GHz to 12.4 GHz With a Nominal 10 dB Gain SMA Female Input*, Pasternack Enterprises, 2017.

[16] D. M. Pozar, *Microwave engineering.* Wiley India, 2017.

[17] R. Montoya Moreno *et al.*, "Beam steerable 26–30 ghz antenna for a fifth generation cellular base station," 2016.

[18] Wshampshire, "W.s. hampshire, inc., hampshire, il," 2019.

[19] M. Taguchi, M. Igasaki, H. Shimoda, and K. Tanaka, "Analysis of arbitrarily shaped dielectric lens antenna by ray tracing method," in *IEEE Antennas and Propagation Society International Symposium. Digest. Held in conjunction with: USNC/CNC/URSI North American Radio Sci. Meeting (Cat. No.03CH37450)*, vol. 3, June 2003, pp. 697–700 vol.3.

[20] P. Piksa, S. Zvanovec, and P. Cerny, "Elliptic and hyperbolic dielectric lens antennas in mmwaves," *Radioengineering*, vol. 20, no. 1, pp. 270–275, 2011.

[21] S. Cornbleet, "Microwave optics. the optics of microwave antenna design." *Pure and Applied Physics*, vol. 41, 1976.

[22] C. Torbitt, J. Venkataraman, and Z. Lu, "Beam shaping and gain enhancement using a diffractive optical element (doe) lens," in *2014 IEEE Antennas and Propagation Society International Symposium (APSURSI)*, July 2014, pp. 767–768.

[23] Rogers, "Rogers corp., chandler, az," 2019.

[24] C. P. Systems, "Chicago plastic systems, inc., crystal lake, il," 2019.

[25] Altium, "Altium llc," 2019.

[26] Q. T. Circuits, "Quick turn circuits, inc., salt lake city, ut," 2019.

[27] S. D. Laboratory, "Space dynamics laboratory, logan, ut," 2019.

[28] Stratasys, "Stratasys ltd., gilbert, az," 2019.